How fragility makes phase-change data storage robust: insights from *ab initio* simulations

Wei Zhang[1,2], Ider Ronneberger[1], Peter Zalden[2,3], Ming Xu[2],
Martin Salinga[2], Matthias Wuttig[2,4], and Riccardo Mazzarello[1,4*]

[1] *Institute for Theoretical Solid State Physics,*
RWTH Aachen University, D-52056 Aachen, Germany

[2] *I. Physikalisches Institut (IA), RWTH Aachen University, D-52056 Aachen, Germany*

[3] *Stanford Institute for Materials and Energy Sciences,*
SLAC National Accelerator Laboratory, Menlo Park, CA 94025, USA

[4] *JARA-FIT and JARA-HPC, RWTH Aachen University, D-52056 Aachen, Germany*

(Dated: August 29, 2014)

In this supplement, (A) we present experimental and theoretical data about the structural properties of amorphous and recrystallized $Ag_4In_3Sb_{67}Te_{26}$ (AIST). More specifically, we compare the calculated X-ray diffraction patterns of the recrystallized models of AIST with experimental data (Fig. S1) and we present the experimental and theoretical extended x-ray absorption fine structure (EXAFS) spectra for both the amorphous and recrystallized phases of AIST (Figs. S2, S3, Table I). Moreover, we show the angle distribution functions (Fig. S4) and the distribution of primitive rings (Fig. S5) of our *ab initio* models of amorphous AIST.

(B) We explain how we calculate the growth velocity by considering the evolution of the number of crystalline-like atoms (Fig. S6). We also discuss how to compute the dot-product, q_4^{dot}, which we use to discriminate between amorphous-like and crystalline-like atoms (Fig. S7).

(C) We explain how the deposition rates k^+ and sticking coefficients S discussed in the main text were calculated (Fig. S8) and provide further details about how the growth velocities v_g included in Table II of the main text were determined.

(D) We present simulations of crystallization of models of AIST containing 540 atoms and low-temperature (400 K) simulations of large models containing 810 atoms.

(E) We provide some technical details about our *ab initio* molecular dynamics (AIMD) simulations and about how we constructed the models of AIST.

A: STRUCTURAL PROPERTIES OF AMORPHOUS AND RECRYSTALLIZED AIST

X-ray diffraction

X-ray diffraction patterns were calculated for the atomic structure of the recrystallized model obtained by *ab initio* molecular dynamics (AIMD) simulations of the crystallization process at 585 K (Fig. S1). A comparison with experimental data shows that the recrystallized models also form a trigonal crystal system (A7). Experiments were performed at room temperature using Cu K-α radiation in grazing incidence to measure the diffracted intensities of a polycrystalline thin film of AIST on a Si substrate. Relative peak intensities in the two patterns are in reasonable agreement. Since all atomic species have very similar

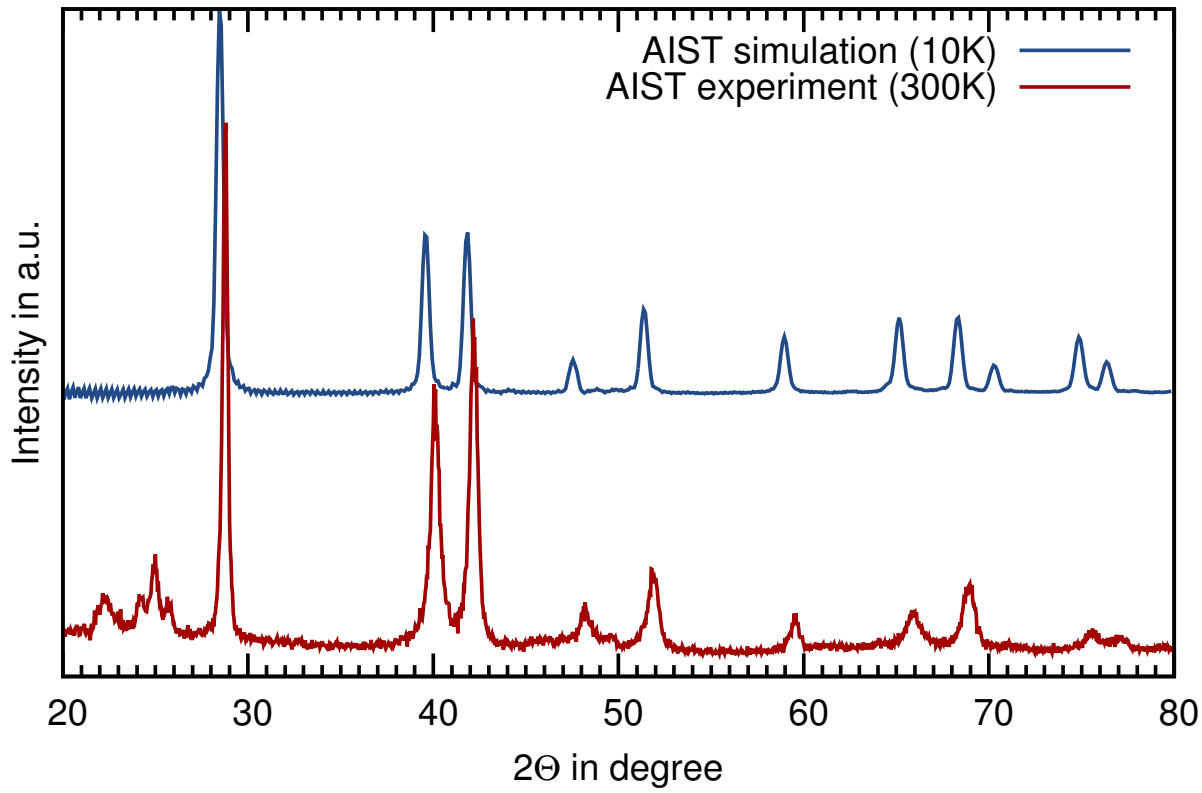

Fig. S1. Theoretical XRD patterns of recrystallized AIST and experimental XRD patterns of oven-crystallized AIST.

atomic numbers, no significant deviations in the peak intensities are expected. Although it is know from the simulations (cf. main text) that all atoms are arranged in a random fashion on the lattice, the similar atomic numbers prevent us from drawing conclusions about the atomic ordering in the experimental sample.

X-ray absorption spectroscopy

In order to obtain chemical contrast and element-specific information on the atomic structure, EXAFS measurements have been performed at beamline CEMO of the accelerator ring DORIS III, as part of Hasylab, DESY. All four K-edges of AIST were measured in transmission geometry on powderous samples pressed to pellets. The samples were cooled to 10 K and measured at least twice to check for statistical deviations between subsequent scans. The resulting data were normalized to pre- and post-edge ranges and Fourier transformed

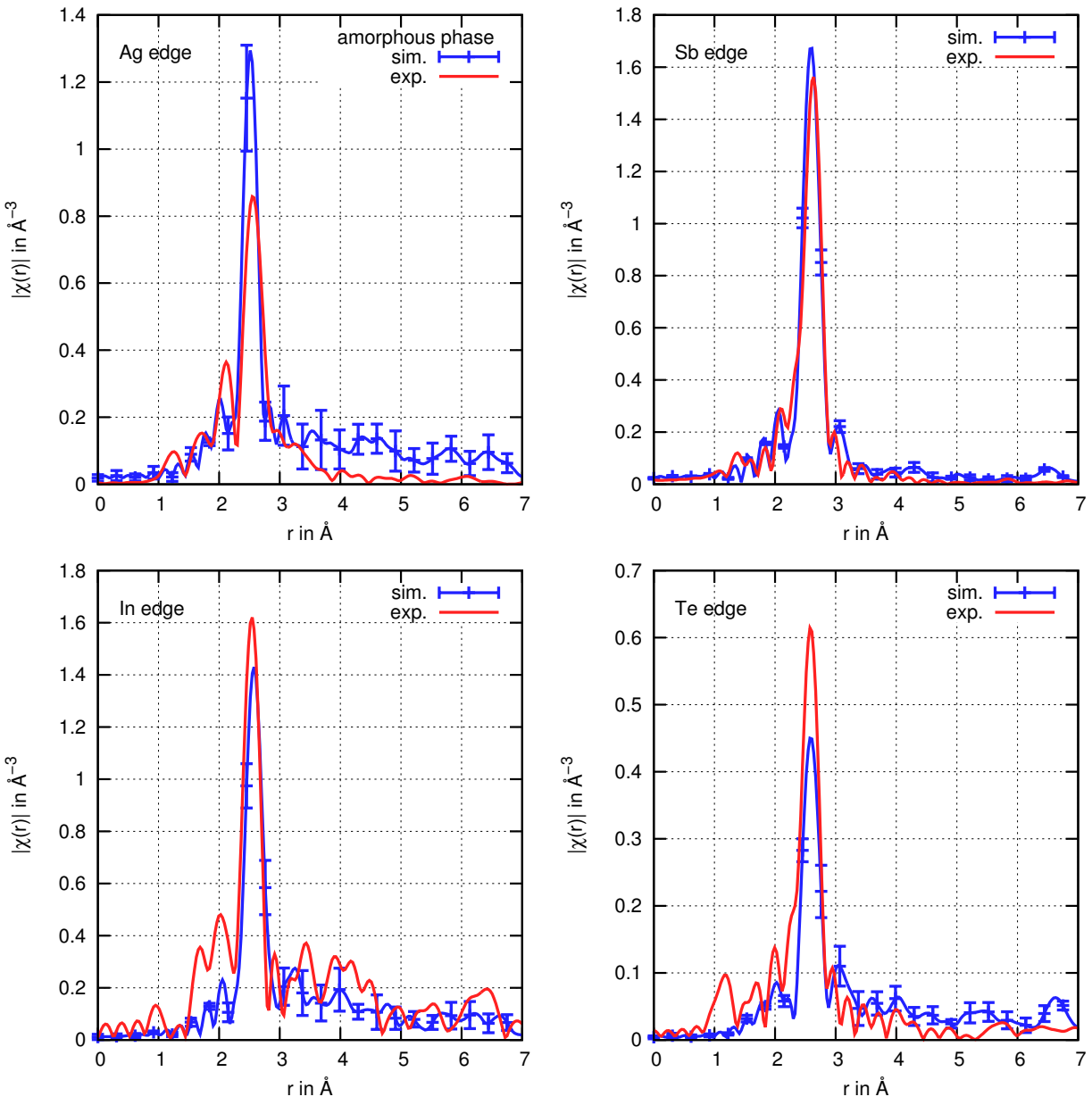

Fig. S2. Fourier transform of experimental EXAFS spectra on the as-deposited amorphous phase and of theoretical spectra on the melt-quenched phase generated by AIMD. All data were obtained from the K absorption edges.

using the computer code Athena [1]. In this way, experimental EXAFS spectra on the as-deposited amorphous and oven-crystallized phases were obtained. They are compared in Figs. S2 and S3 with simulated data from the AIMD models of melt-quenched amorphous and re-crystallized phases. Since the EXAFS measurements were performed at T

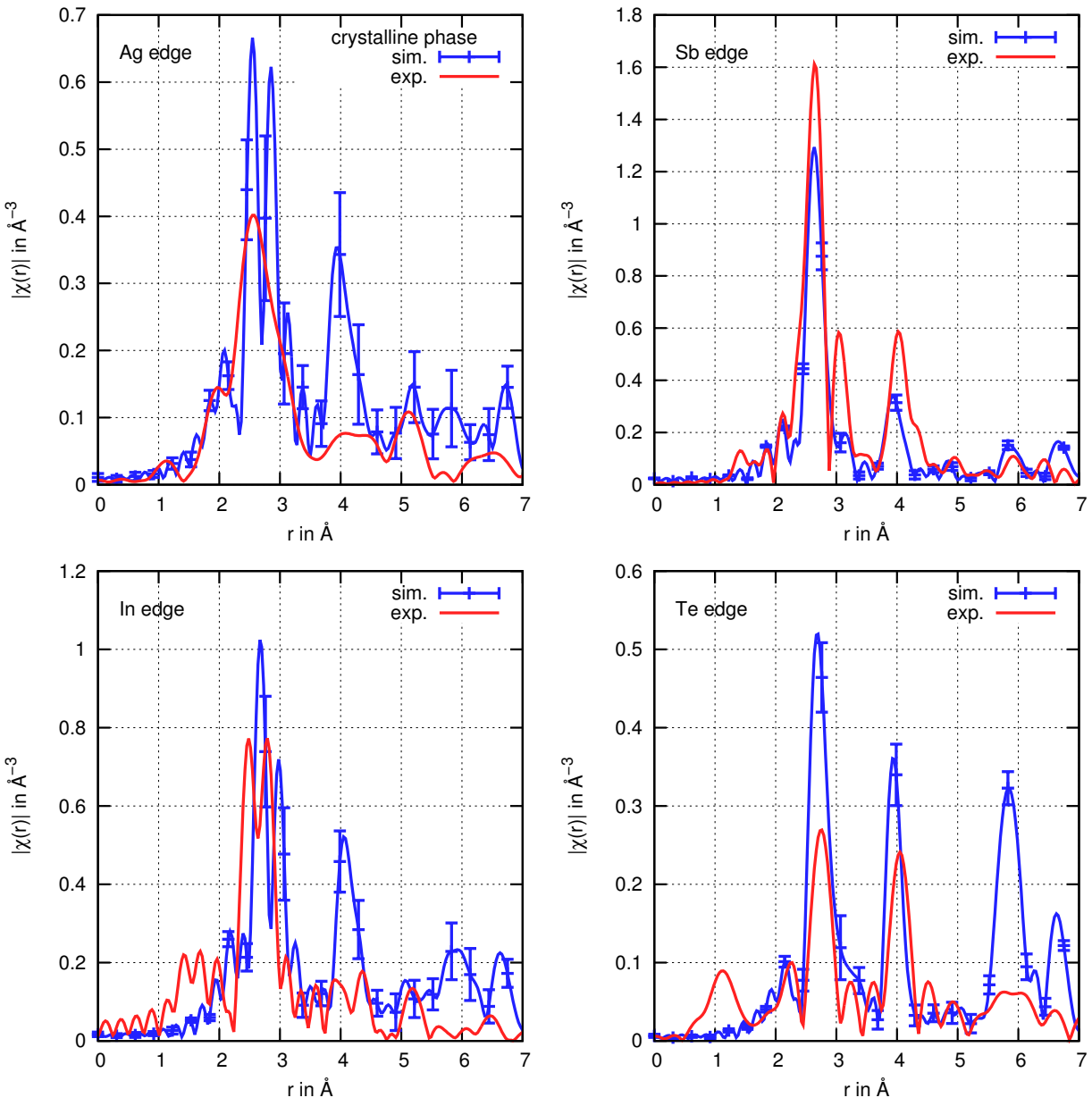

Fig. S3. Fourier transform of experimental EXAFS spectra on the oven-crystallized phase (annealed at 510 K) and of theoretical EXAFS spectra on the recrystallized phase obtained by AIMD. All data were obtained from the K absorption edges.

= 10 K, AIMD simulations were carried out at this temperature as well. As regards the theoretical spectra, the atomic coordinates of 36 AIMD steps were used to calculate the absorption spectra of each individual atom. All possible multiple scattering effects were taken into account, as implemented in the state-of-the-art FEFF 8.4 [2] computer code.

Atom	r_{EXAFS} (Å)	N_{EXAFS}	σ^2 in Å^2	E_0 in eV
		Amorphous		
Ag	2.81(1)	4.0 ± 0.7	0.007(1)	3.0(5)
In	2.82(1)	2.7 ± 0.5	0.002(1)	4(2)
Sb	2.87(1)	3.4 ± 0.6	0.0025(3)	9.7(4)
Te	2.83(1)	1.6 ± 0.4	0.0034(3)	9.4(3)
		Crystalline		
Ag	2.84(3), 3.02(3)	7.2 ± 0.7	0.010(6), 0.011(8)	0.9(8)
In	2.80(1), 2.99(1)	6.6 ± 0.7	0.006(1), 0.004(1)	2.3(8)
Sb	2.89(1), 3.32(1)	6.2 ± 0.6	0.002(1), 0.006(1)	6.0(3)
Te	2.94(1), 3.39(3)	3.8 ± 0.5	0.007(2), 0.019(6)	4.9(7)

TABLE I. The nearest neighbour bond lengths (1st column) and coordination numbers (2nd column) for as-deposited amorphous and oven-crystallized AIST, obtained from EXAFS experiments. In the 3rd and 4th column, the edge shift E_0 and the Debye-Waller parameter σ^2 of each path are shown (see text). Numbers in paranthesis indicate the statistical error on the last digit.

Thermal broadening effects were already contained in the atomic coordinates as a result of AIMD and, therefore, no further model for the vibrational states was required to match the experimental and calculated spectra. The absorption spectra of each chemical species were summed/averaged until a convergence of at least 5 % was achieved for the least abundant element. This required averaging at least 500 spectra per atomic species. The energy difference between the calculated and experimental Fermi level was corrected for, based on a refinement of the scattering paths in the experimental data (cf. Table I). The resulting data were Fourier transformed over the same energy range as the experimental data to allow for direct comparison.

All experimental data were also refined by the scattering path expansion method, as implemented in the computer code Artemis [1]. Due to the similar atomic numbers, the chemical contrast originates solely from the nature of the absorber atom, not from the backscattering atom. In consequence, it does not matter which atomic species of AIST is assumed to facilitate the backscattering of the photoelectrons, but for completeness we mention that we simulated Sb (the most abundant atom) at the Ag, In and Te edges and

Te (the second most abundant atom) at the Sb edge. All results from a refinement of the scattering paths in the first shell are compiled in Table I. The treatment involves the energy difference between simulations and experiments, E_0 (edge shift), the Debye-Waller parameter of each path σ^2, a coordination number N and an interatomic distance r_i. In the absence of reference data for a well crystallized structure, the central atom loss factor, S_0^2, was set to 0.7 for all data sets to extract the coordination numbers. The resulting systematic error of about 10% was included in the presentation of the coordination numbers (CNs).

A comparison between experimental data and computational results for the amorphous phase is presented in Fig. S2, which shows that the bond lengths deviate by less than 3 %. One should note that the peak heights in EXAFS are dominated by the atomic disorder at the given distance and, to a smaller extent, influenced by the CNs. In this respect, the disorder around In and Sb atoms is perfectly reproduced, whereas discrepancies are observed for Ag and Te atoms. These deviations indicate that the Te (resp. Ag) atoms have a higher (resp. lower) ordering tendency in the measured, as-deposited sample. Also the theoretical and experimental CNs overlap within the experimental error, except for Te, which has a higher coordination in the simulated amorphous phase.

The comparison of the experimental and theoretical bond lengths in the crystalline phase reveals a good agreement for Ag, Sb and Te, but deviations of the order of 5-6 % occur for In atoms. This might be partially due to the small number of In atoms (24) in our AIMD models and the consequent poor statistics. For all elements except Sb, the atomic order resulting from the simulated (fast) crystallization is higher than the ordering after (slow) crystallization in an oven. This is surprising, in that the recrystallized AIMD models contain a large amount of compositional Sb/Te disorder. In particular, the atomic structure around Te atoms shows pronounced differences in ordering at large values of r. Sb is 6-fold coordinated, which corresponds to the average coordination of an A7 lattice. The CNs obtained from EXAFS analysis show that the dopant atoms, Ag and In, mostly seem to occupy lattice or interstitial sites, i.e. the CNs are higher than 6 but are not as high as in a phase separated material. Since bond lengths around interstitial atoms are known to be much shorter, the bigger deviation of average bond length around In atoms may be partially due to fact that there exists the higher amount of interstitial In in experiments than in simulations. Experimental data indicate that Te atoms have an average CN significantly lower than 6. AIMD simulations yields larger values, although one should keep in mind

that the computed CNs depend very sensitively on the cutoff radius chosen. It is worth mentioning that the experimental value of the CN of Te obtained from the present analysis (3.8(5)) is in good agreement with earlier studies by Tashiro et al. [3] and with diffraction based experiments by Agafonov *et al.* [4] for Sb_2Te, where Te atoms were found to be 4-fold coordinated on average. According to Agafonov, however, the average coordination of Sb would be 4-fold, which does not match the present results for crystalline AIST.

As a last remark of this section, we would like to point out that, in principle, the different dynamical properties of the amorphous phases quenched at different rates (see Fig. 3(a) of the main text) should depend on structural differences. It is noted, however, that the experimental data discussed here refer to the as-deposited phase, which exhibits a dynamical behavior deviating greatly from the melt-quenched phase [5].

Angle and ring distribution functions

In order to have a better understanding of bonding in amorphous AIST, we also computed the angular distribution functions (ADFs), shown in Fig. S4. The ADFs were obtained by averaging over a 30 ps MD trajectory at 300K. The ADFs exhibit a large peak at 90^o and a small peak around 165^o, which indicate that most atoms are in a (defective) octahedral-like configuration, similarly to the clean phase of Sb_2Te [6]. For impurity atoms, the angular distribution is broader due to the relatively poor statistics.

Now we turn to the discussion of the medium range order. The distribution of primitive rings in amorphous AIST is shown in Fig. S5. Five-fold rings are dominant (18%), followed by four-fold (13%) and six-fold (10%) rings. The distribution is similar to that of the clean phase of Sb_2Te but different from that of the well-studied Sb-Te compound Sb_2Te_3, where four-fold rings are dominant [6]. It is worth mentioning that the ring statistics of AIST is also similar to that of Ag- and In-doped Sb_4Te alloys [7].

B: CALCULATION OF THE GROWTH VELOCITY, DOT PRODUCT ORDER PARAMETER

As mentioned in the main text, we calculated the growth velocity by computing the evolution of the number of crystalline-like atoms, N_c, see Fig. S6. This can be done because

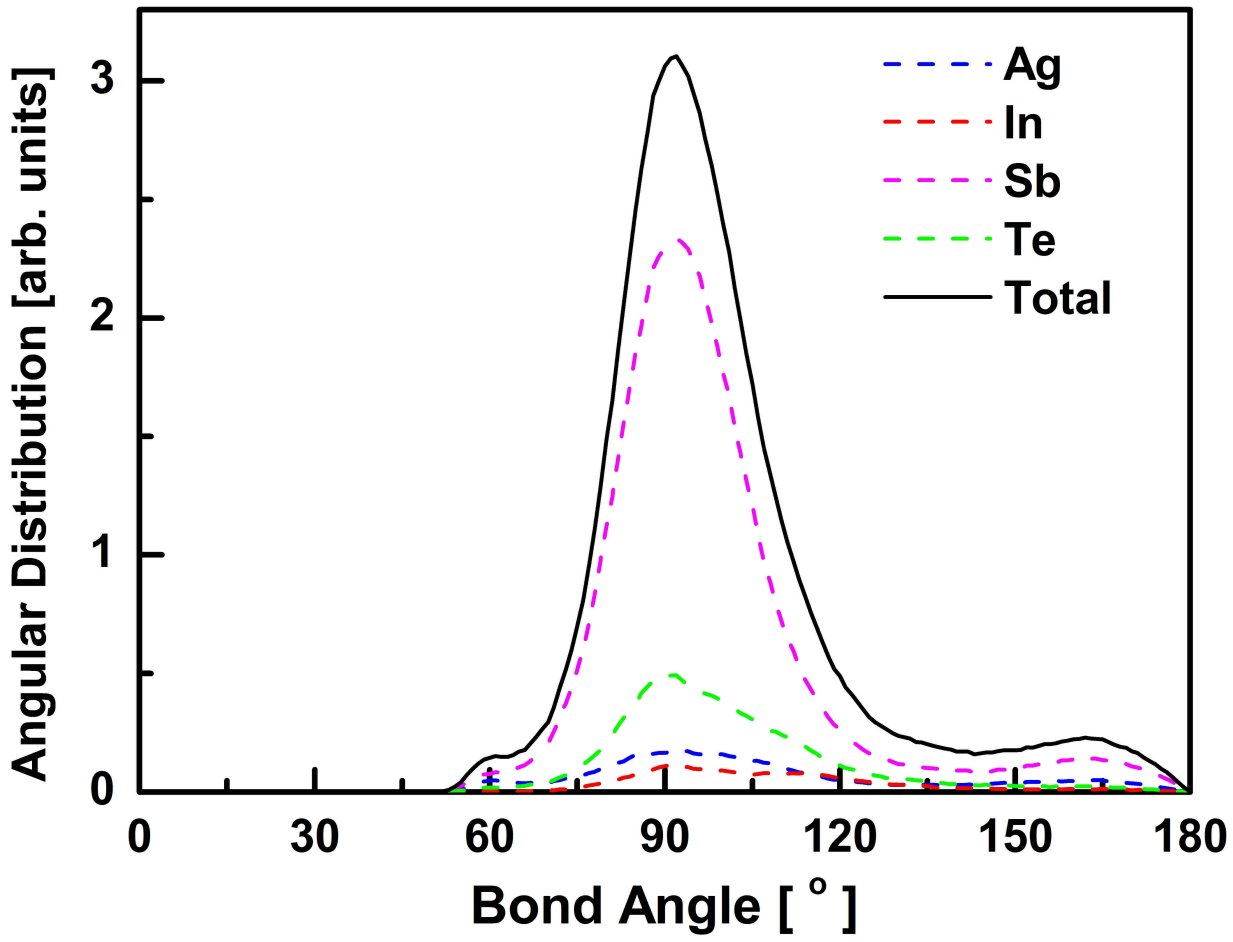

Fig. S4. Angle distribution functions of amorphous AIST.

crystallization occurs via crystal growth at the crystalline-amorphous interface, i.e. new crystalline-like atoms appear near the interface only. Therefore, the ratio $N_c(t)/N$ (where N is the total number of atoms) describes the evolution of the interface along the growth direction (x-axis) as a function of time. By multiplying this ratio by the x-axis cell parameter and dividing by the corresponding time t, one obtains v_g. To distinguish crystalline-like and amorphous-like atoms, we employ the bond order parameter q_4^{dot}, defined below.

The local Steinhardt order parameter $q_l(i)$ is defined as a rotationally invariant norm of the local bond order function $q_{lm}(i)$:

$$q_l(i) = \sqrt{\frac{4\pi}{2l+1} \sum_{m=-l}^{l} |q_{lm}(i)|^2}, \tag{1}$$

where $q_{lm}(i)$ is chosen to be the average value of the spherical harmonics in the neighbour-

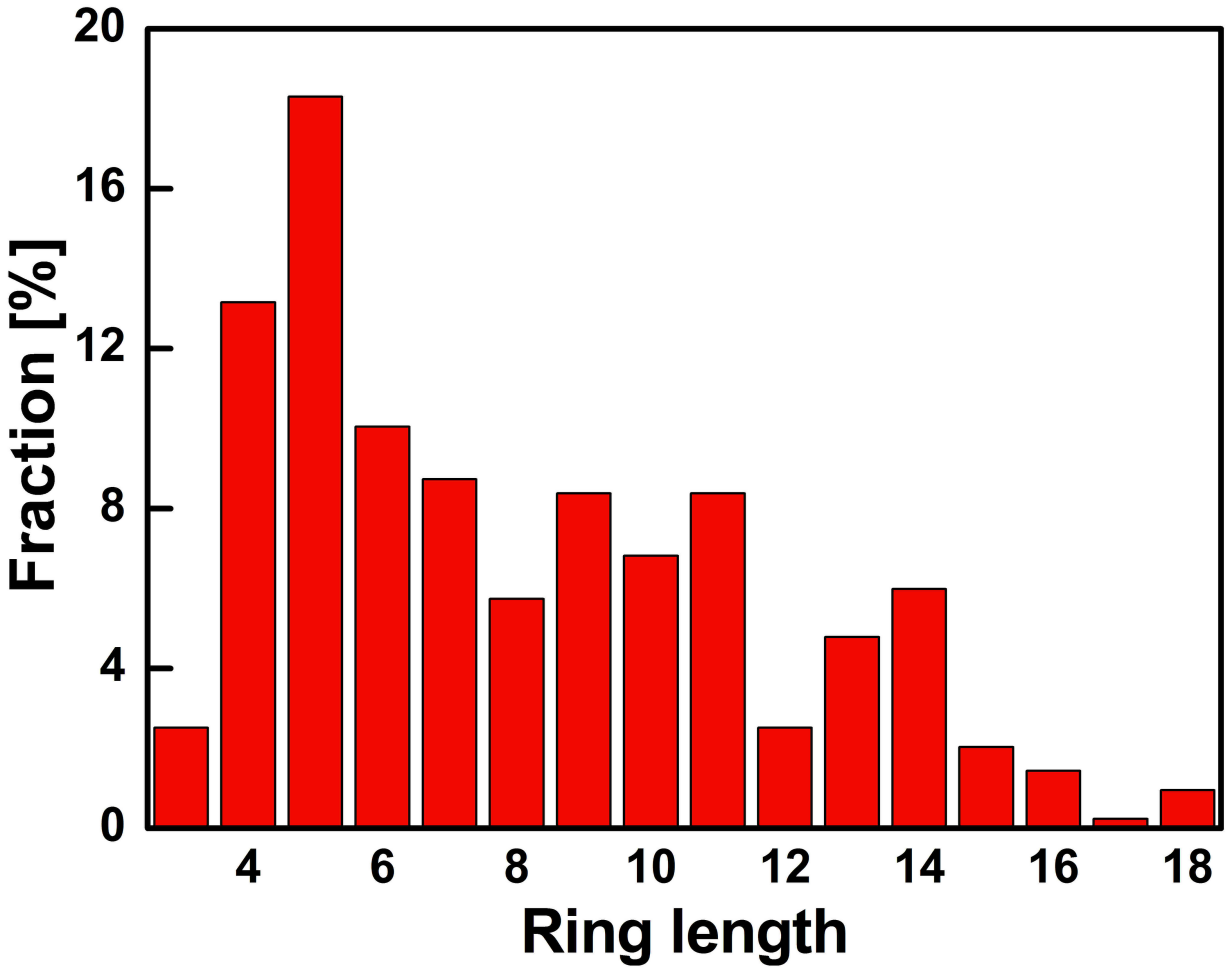

Fig. S5. Statistics of primitive rings for amorphous AIST.

hood Ω_i of the atom i,

$$q_{lm}(i) = \frac{1}{N_i} \sum_{j \in \Omega_i} f(r_{ij}) Y_{lm}(\hat{\mathbf{r}}_{ij}). \tag{2}$$

The spherical harmonics $Y_{lm}(\hat{\mathbf{r}}_{ij})$ depend only on the relative orientation of the vector $\mathbf{r}_{ij} = \mathbf{r}_i - \mathbf{r}_j$ connecting the atom i to its neighbour j and the average over the N_i atoms in the neighbourhood Ω_i is smoothened by a radial cutoff function f:

$$f(r_{ij}) = \frac{1 - \left(\frac{r_{ij}}{r_c}\right)^{p_1}}{1 - \left(\frac{r_{ij}}{r_c}\right)^{p_2}}, \tag{3}$$

where r_c is a cutoff radius and $p_1 < p_2$ are suitably chosen exponents yielding a sufficiently sharp cutoff function.

One can simplify the notation by introducing a $(2l+1)-$dimensional vector $\mathbf{q}_l(i)$, the

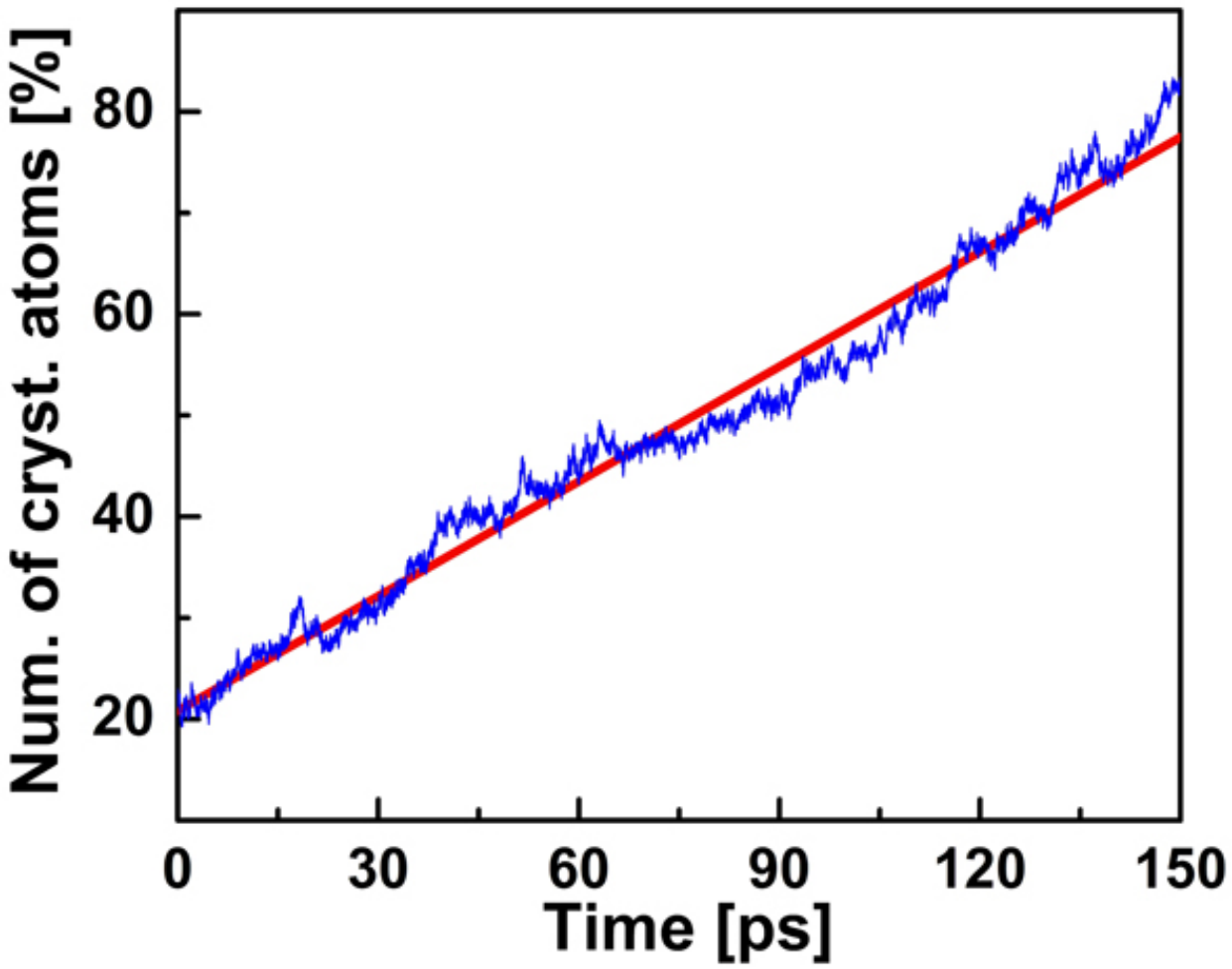

Fig. S6. Evolution of the number of crystalline-like atoms during crystallization of the 810-atom model of AIST at 585 K (blue line). The red straight line indicates the linear regression of the blue line. In the last part of the trajectory, corresponding to $t > 150$ ps, the interaction between the two amorphous-crystalline interfaces is significant. Hence, these data were removed from the linear regression.

components of which are the q_{lm} values:

$$\mathbf{q}_l(i) = \begin{pmatrix} q_{l,l} \\ q_{l,l-1} \\ \ldots \\ q_{l,-l+1} \\ q_{l.l} \end{pmatrix} = (q_{lm}(i))_{m=-l,l}\,. \tag{4}$$

Then $q_l(i)$ can be written as:

$$q_l(i) = \sqrt{\frac{4\pi}{2l+1}} \left\| \mathbf{q}_l(i) \right\| . \tag{5}$$

The new order parameter $q_l^{dot}(i)$ is constructed from the so called bond order correlations C_{ij} between neighboring atoms, which were first introduced by Frenkel and coworkers to analyze the solid-like connections between particles. The bond order correlations C_{ij} are defined as the dot product of the vector $\mathbf{q}_l(i)$ with the complex conjugate of $\mathbf{q}_l(j)$, divided by the rotationally invariant norms of the two vectors:

$$C_{ij} = \frac{\mathbf{q}_l(i) \cdot \mathbf{q}_l^*(j)}{\left\| \mathbf{q}_l(i) \right\| \left\| \mathbf{q}_l(j) \right\|}. \tag{6}$$

We define $q_l^{dot}(i)$ as the average of the C_{ij}'s taken in the neighborhood Ω_i, in a similar fashion as for $q_l(i)$,

$$q_l^{dot}(i) = \frac{1}{N_i} \sum_{j \in \Omega_i} C_{ij}, \tag{7}$$

and employ it as an order parameter to characterize each atom.

For solid-like particles, the average correlation of the bond order to its neighbours will take values close to one, whereas for particles with disordered surrounding it has values around zero. The local symmetry of the solid phase determines the value of the bond order parameter q_l. To ensure that the typical values of q_l in the two phases differ significantly, one has to select a suitable angular momentum l.

Using the parameters $l = 4$, $p_2 = 2 \cdot p_1 = 24$ and $r_c = 4$ Å, the dot product can nicely discriminate between the crystalline and amorphous phase of AIST, as shown in Fig. S7.

C: CALCULATION OF DEPOSITION RATES AND STICKING COEFFICIENTS

As discussed in the main text, we calculated the deposition rate k^+ and the sticking coefficient S near the crystalline-amorphous interface. The sticking process is visualized in Fig. S8. At the interface, there are several empty crystalline sites, where the atoms can jump from the amorphous phase. After occupying the site, the atoms can either form stable bonds with the nearest-neighbour atoms of the crystalline interface (thereby becoming part of the crystal) or escape. We counted the total number of landing n_l and escaping n_e events within the interface region during the whole growth process and computed the rate k^+ as the number of landing events per unit of time and the coefficient S as $(n_l - n_e)/n_l$.

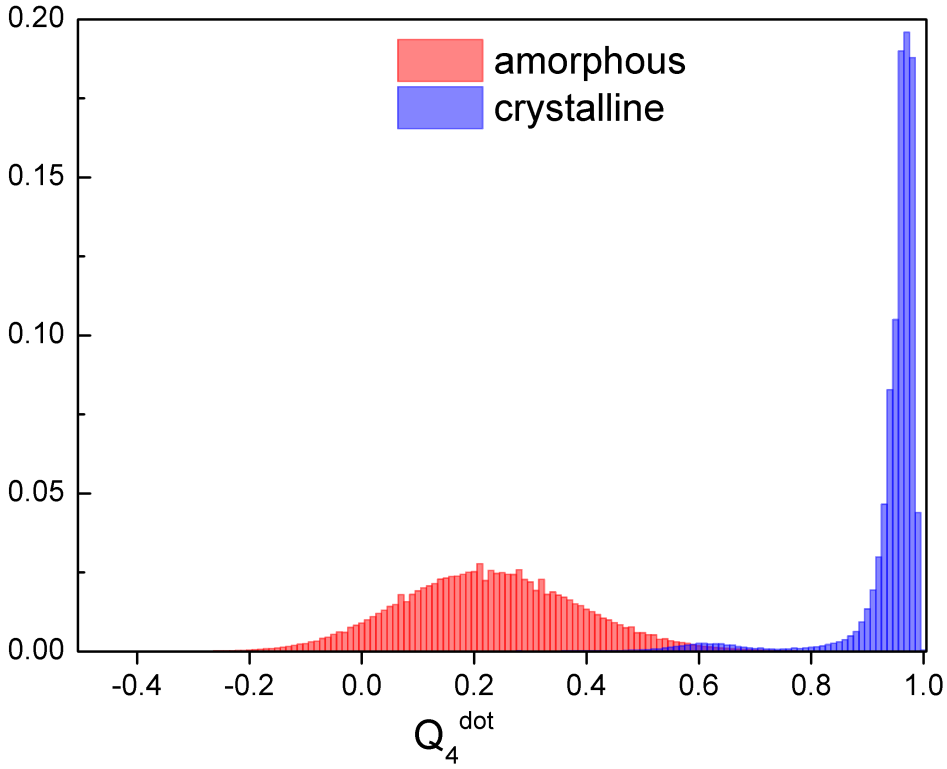

Fig. S7. Distribution of the values of $q_4^{dot}(i)$ for amorphous and crystalline AIST.

In the following, we provide some technical details about the calculation of k^+ and S. Firstly, we defined the crystalline sites as small spheres with a cutoff radius R, centered at the final positions of the atoms in the fully recrystallized phase. The radius R was chosen to be equal to twice the mean squared displacement (MSD) of the atoms in the crystalline phase at the target T, calculated from a MD trajectory. Although the absolute values of k^+ and S, as well as k^+S, will obviously depend on the value of R, the temperature dependence of the product k^+S is weakly affected by the choice of R (for reasonable values of R ranging from the MSD of the atoms to twice this quantity). Secondly, we defined the time T_{END} at which a crystalline site is no longer available for hopping, in that it is stably occupied by an atom. Thirdly, we determined the time T_{START} at which a crystalline site started to be available for an atom to hop. For a given crystalline site, T_{START} was set to be equal to the time at which at least one nearest neighbour crystalline site became occupied by an atom. Hence, T_{END} and T_{START} of nearest-neighbour sites are generally correlated. In other

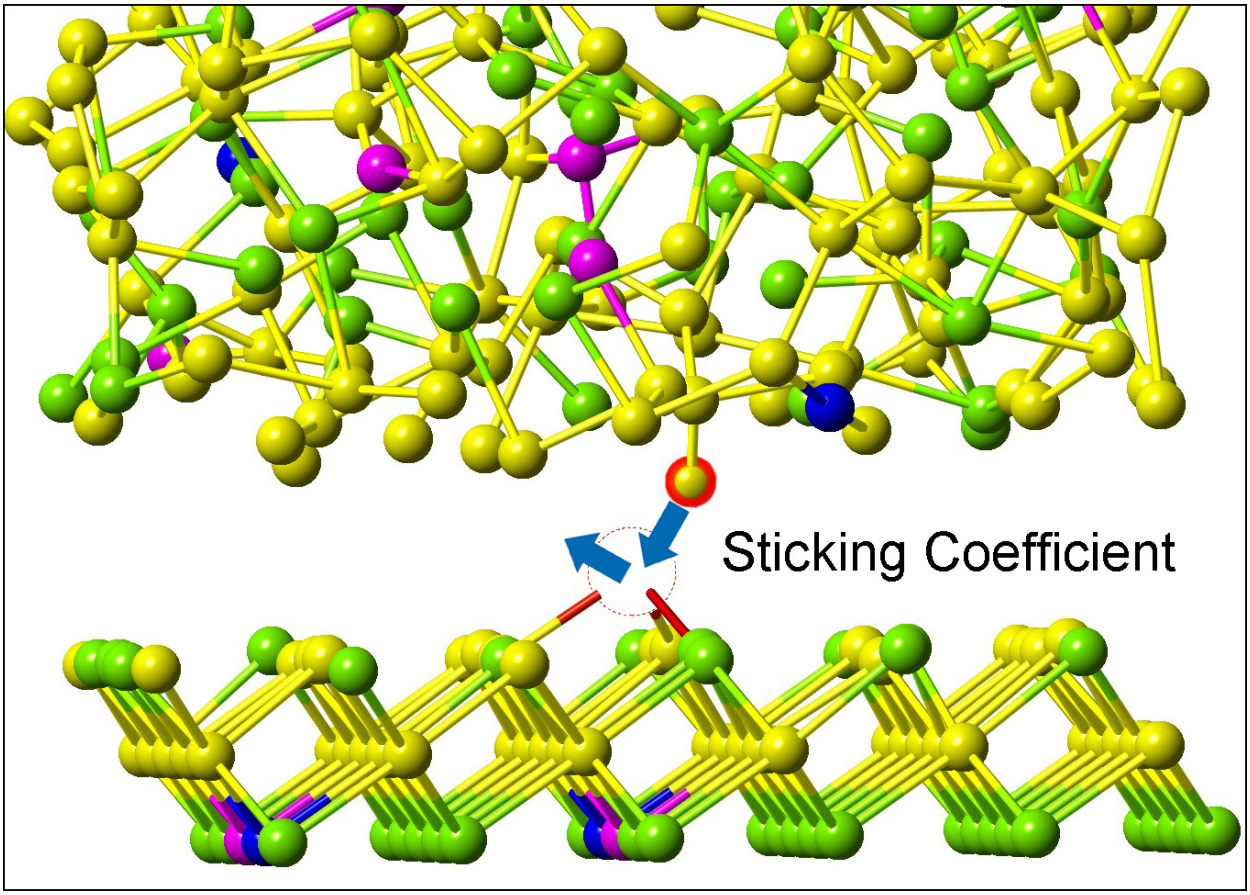

Fig. S8. Sticking process at the crystalline-amorphous interface. The gap between the liquid and the crystalline region is increased for the purpose of visualization.

words, T_{START} of a site always coincides with T_{END} of one of its nearest-neighbour sites. To evaluate the deposition rate k^+, we calculated the averaged time interval τ between the T_{START} of a site and the first landing event. The inverse of this quantity is equal to k^+. As regards S, we simply counted the numbers n_l and n_e for each site, between T_{START} and T_{END}.

Once k^+ and S are computed from the AIMD trajectories, the growth velocity can be evaluated as $v_g = \lambda k^+ S$, where λ is a constant factor having the unit of length (we used λ = 1.7 Å). The corresponding v_g were compared with the velocities computed directly from the trajectories in Table II of the main text. The ratio between the two velocities varies by about 20 % in the temperature range 585 K - 455 K. Hence, the agreement is quite good, despite the simplicity of the method used to evaluate k^+ and S. In Table II, we also included

the growth velocities obtained from WF formula,

$$v_g(T) = \frac{6D(T)}{\tilde{\lambda}} \left[1 - \exp\left(-\frac{\Delta\mu(T)}{k_{\mathrm{B}}T} \right) \right], \tag{8}$$

where $D(T)$, the bulk diffusivity, is calculated from the AIMD trajectories of the amorphous models of AIST (without crystallization seeds) and $\Delta\mu(T)$ is estimated using Thompson-Spaepen formula [8],

$$\Delta\mu(T) = \Delta H_m \frac{T_m - T}{T_m} \frac{2T}{T_m + T}. \tag{9}$$

The experimental values [9] for the heat of fusion $\Delta H_m = 173$ meV/at and the melting temperature $T_m = 808$ K were employed. We used $\tilde{\lambda} = 1.7$ Å in Formula (8) as well.

D: SIMULATIONS OF CRYSTALLIZATION OF SMALL MODELS AND LOW-TEMPERATURE SIMULATIONS

In this section, we present a) simulations of crystallization of a model of AIST containing 540 atoms and b) low-temperature (400 K) simulations of a large model (810 atoms).

Some snapshots of the crystallization trajectory of the small AIST model at T = 585 K are shown in Fig. S9. A plot of the evolution of the number of crystalline-like atoms during crystallization is also shown. The resulting growth velocity is by 16 % smaller than the average value shown in Fig. 3a.

In Fig. S10, two snapshots of the low temperature simulation of the large model are shown, corresponding to the initial stage of crystallization and to the structure obtained after 280 ps. Roughly 4 additional crystalline layers are observed in the second snapshot, corresponding to a growth velocity of about 1 m/s.

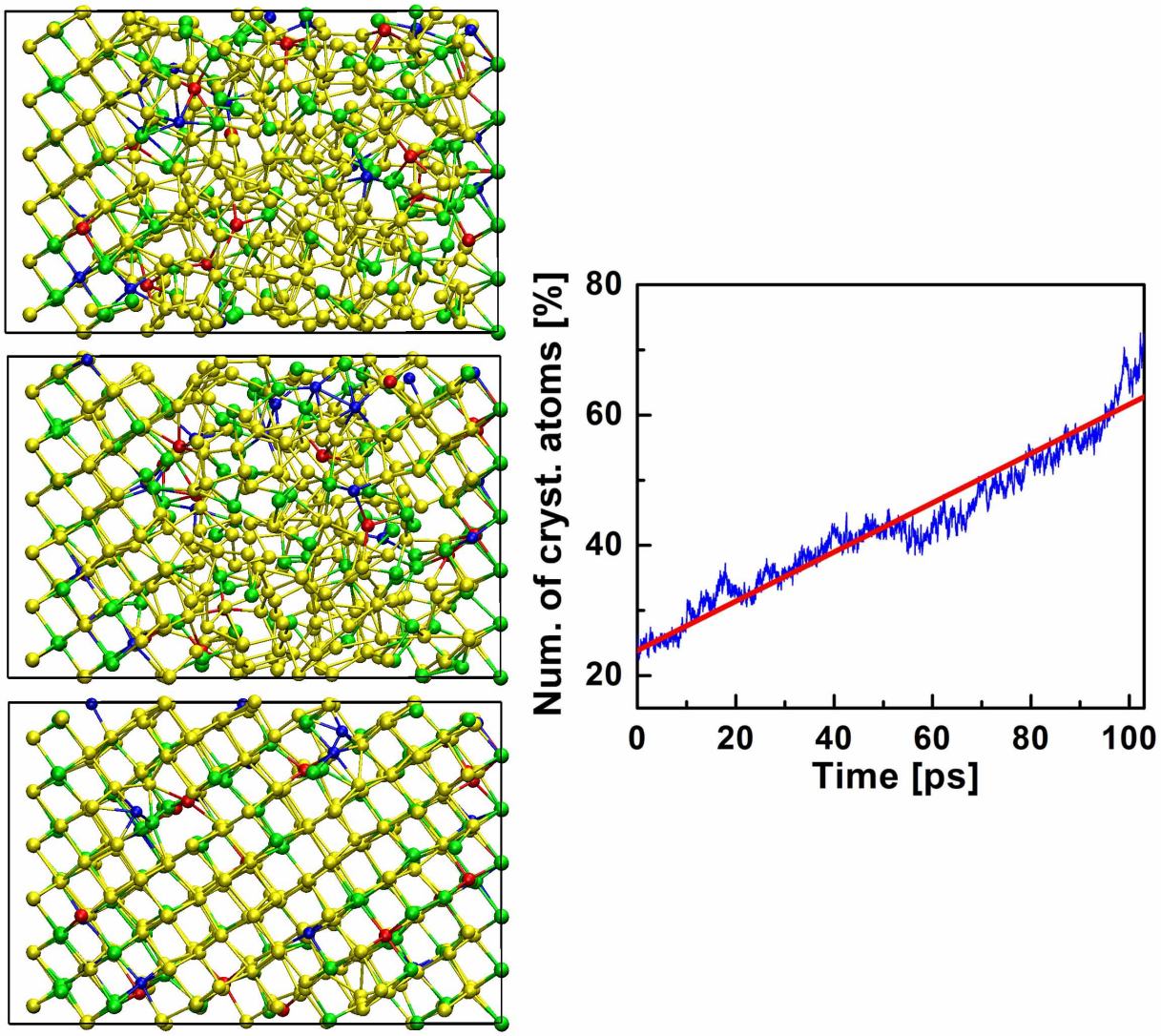

Fig. S9. (Left) Crystallization of a small model of AIST, containing 540 atoms, at T = 585 K. The three snapshots are taken at 0, 60 and 120 ps, respectively. (Right) Evolution of the number of crystalline particles during the process and corresponding linear fit used to extract the growth velocity. The last 20 ps of the trajectory were discarded due to the spurious effects stemming from the interaction between the two interfaces.

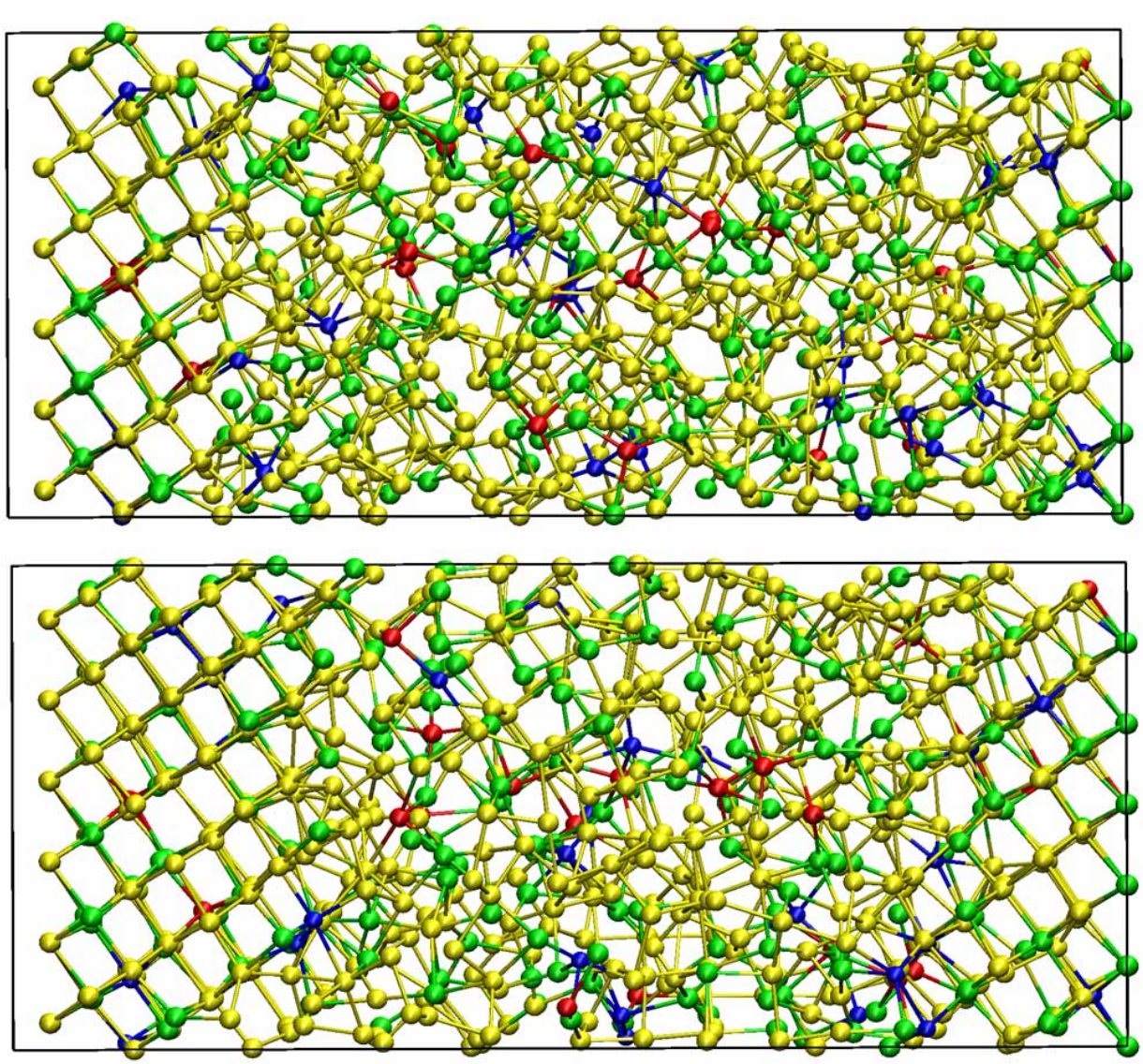

Fig. S10. Crystallization of a 810-atoms model of AIST at T = 400 K. Snapshots are taken at 0 and 280 ps.

E: SIMULATION DETAILS AND MODEL CONSTRUCTIONS

The molecular dynamics simulations were carried out using QUICKSTEP [10], a code based on a mixed Gaussian and plane-wave approach included in the CP2K package [11]. We employed the "second-generation" Car-Parrinello scheme [12]. The generalized gradient approximation (GGA) to the exchange-correlation potential [13] and scalar-relativistic

Goedecker pseudopotentials [14] were used. The Kohn-Sham orbitals were expanded in a triple-zeta plus polarization Gaussian-type basis set, whereas the charge density was expanded in plane waves with a cutoff of 300 Ry. The Brillouin-zone was sampled at the point of the supercell. The time step for the simulations was 2 fs.

The models with and without crystalline boundaries were heated at 3000 K and then cooled down to the melting temperature T_m (900 K), at which they were equilibrated for 30 ps. They were then quenched to 300 K within 30 ps, and equilibrated there for another 30 ps. To investigate the crystallization properties of the models, we subsequently increased T to the target temperature with very fast heating rate and performed canonical (NVT) simulations. For the investigation of the structural properties, they amorphous models were instead quenched down to 10 K and further relaxed to 0 K. The amorphous models without crystallization seeds were generated both at the crystalline density and at the amorphous density [15]. The structural properties of the latter models were compared with EXAFS measurements.

* Corresponding author. Email address: mazzarello@physik.rwth-aachen.de

[1] B. Ravel, M. Newville, *J. Synchrotron Rad.* **12**, 537 (2005).

[2] A. L. Ankudinov, B. Ravel, J. J. Rehr, S.D. Conradson, *Phys. Rev. B* **58**, 7565 (1998).

[3] H. Tashiro, M. Harigaya, Y. Kageyama, K. Ito, M. Shinotsuka, K. Tani, S. Emura, *Jpn. J. Appl. Phys.* **41**, 3758 (2002).

[4] V. Agafonov, N. Rodier, R. Céolin, R. Bellissent, C. Bergman, J. P. Gaspard, *Acta Crystallogr. Sect. C* **47**, 1141 (1991).

[5] M. Salinga, E. Carria, A. Kaldenbach, M. Bornhöfft, J. Benke, J. Mayer, M. Wuttig, *Nature Comm.* **4**, 2371 (2013).

[6] W. Zhang, I. Ronneberger, Y. Li , R. Mazzarello, *Monatsh. Chem.* **145**, 97 (2014).

[7] T. Matsunaga, J. Akola, S. Kohara, T. Honma, K. Kobayashi, E. Ikenaga, R. O. Jones, N. Yamada, M. Takata, R. Kojima, *Nature Mater.* **10**, 129 (2011).

[8] C. V. Thompson, F. Spaepen, *Acta Metall. Mater.* **27**, 1855 (1979).

[9] J. A. Kalb, Ph.D. thesis (RWTH Aachen University, Aachen, 2006).

[10] J. VandeVondele, M. Krack, F.Mohamed, M. Parrinello, T. Chassaing and J. Hutter *Compu. Phys. Commun.* **167**, 103 (2005).

[11] J. Hutter, M. Iannuzzi, F. Schiffmann and J. VandeVondele *Wiley Interdiscip. Rev. Comput. Mol. Sci.* **4**, 15 (2014). www.cp2k.org.

[12] T. D. Kühne, M. Krack, F. R. Mohamed and M. Parrinello, *Phys Rev. Lett.* **98**, 066401 (2007).

[13] J. P. Perdew, K. Burke and M. Ernzerhof, *Phys. Rev. Lett.* **77**, 3865 (1996).

[14] S. Goedecker, M. Teter and J. Hutter, *Phys. Rev. B* **54**, 1703 (1996).

[15] W. K. Njoroge and M. Wuttig, *J. Appl. Phys.* **90**, 3816 (2001).